



**20<sup>th</sup> IAEA Fusion Energy Conference  
Vilamoura, Portugal, 1-6 November 2004**

---

**IAEA-CN-116/TH/4-1**

**Mechanisms for ITB Formation and Control  
in Alcator C-Mod Identified through  
Gyrokinetic Simulations of TEM Turbulence**

D. R. Ernst, N. Basse, P. T. Bonoli, P. J. Catto, W. Dorland,<sup>†</sup>  
C. L. Fiore, M. Greenwald, A. E. Hubbard, E. S. Marmor,  
M. Porkolab, J. E. Rice, K. Zeller and K. Zhurovich

Plasma Science and Fusion Center  
Massachusetts Institute of Technology  
Cambridge, Massachusetts, USA

<sup>†</sup> Department of Physics  
University of Maryland  
College Park, Maryland, USA

---

This is a preprint of a paper intended for presentation at a scientific meeting. Because of the provisional nature of its content and since changes of substance or detail may have to be made before publication, the preprint is made available on the understanding that it will not be cited in the literature or in any way be reproduced in its present form. The views expressed and the statements made remain the responsibility of the named author(s); the views do not necessarily reflect those of the government of the designating Member State(s) or of the designating organization(s). In particular, neither the IAEA nor any other organization or body sponsoring this meeting can be held responsible for any material reproduced in this preprint.

## Mechanisms for ITB Formation and Control in Alcator C-Mod Identified through Gyrokinetic Simulations of TEM Turbulence

D. R. Ernst, N. Basse, P. T. Bonoli, P. J. Catto, W. Dorland,<sup>†</sup> C. L. Fiore, M. Greenwald, A. E. Hubbard, E. S. Marmor, M. Porkolab, J. E. Rice, K. Zeller and K. Zhurovich

Plasma Science and Fusion Center, Mass. Inst. of Technology, Cambridge, MA, USA

<sup>†</sup>Department of Physics, Univ. of Maryland, College Park, MD, USA

e-mail contact of main author: dernst@psfc.mit.edu

**Abstract.** Internal particle and thermal energy transport barriers are produced in Alcator C-Mod with off-axis ICRF heating, with core densities exceeding  $10^{21} \text{ m}^{-3}$ , without core fueling, and with little change in the temperature profile. Applying on-axis ICRF heating controls the core density gradient and rate of rise. The present study employs linear and nonlinear gyrokinetic simulations of trapped electron mode (TEM) turbulence to explore mechanisms for ITB formation and control in Alcator C-Mod ITB experiments. Anomalous pinches are found to be negligible in our simulations; further, the collisional Ware pinch is sufficient to account for the slow density rise, lasting many energy confinement times. The simulations have revealed new nonlinear physics of TEM turbulence. The critical *density* gradient for onset of TEM turbulent transport is nonlinearly up-shifted by zonal flows. As the density profile peaks, during ITB formation, this nonlinear critical gradient is eventually exceeded, and the turbulent particle diffusivity from GS2 gyrokinetic simulations matches the particle diffusivity from transport analysis, within experimental errors. A stable equilibrium is then established when the TEM turbulent diffusion balances the Ware pinch in the ITB. This equilibrium is sensitive to temperature through gyroBohm scaling of the TEM turbulent transport, and the collisionality dependence of the neoclassical pinch, providing for control of the density rate of rise with on-axis RF heating. With no core particle fueling, and  $\sim 1$  mm between density spatial channels, the C-Mod experiments provide a nearly ideal test bed for particle transport studies. The pure TEM is the only unstable drift mode in the ITB, producing particle transport driven by the density gradient.

### 1. Introduction

This paper summarizes gyrokinetic turbulence simulation work [1, 2] carried out to address ITB formation and control in Alcator C-Mod experiments. Extensive nonlinear gyrokinetic simulations of purely density gradient driven, trapped electron mode (TEM) turbulence are carried out. The simulations have revealed a new nonlinear upshift in the critical density gradient for the onset of TEM turbulence, similar to the Dimits shift in the critical temperature gradient for toroidal ITG mode turbulence [3]. Mechanisms for ITB formation and control are identified through microstability analysis, transport analysis, and nonlinear gyrokinetic turbulence simulations. Trapped electron modes are found to play a key role in limiting the density gradient. The neoclassical pinch is sufficient to form the ITB. No significant turbulence induced net particle pinch, relevant to ITB formation, is evident. The electron particle and thermal energy transport from nonlinear GS2 [4] simulations match experiment, in the ITB steep density gradient region, within experimental and statistical errors.

Internal transport barriers form in Alcator C-Mod single-null enhanced  $D\alpha$  H-Mode plasmas, in the presence of intense off-axis minority ion-cyclotron resonant heating [5, 6, 7], immediately following the H-mode transition. Internal barriers also form during H-Mode back-transitions [7], and in plasmas with pure Ohmic heating [8]. Barrier formation is characterized by a slow rise of the core density over many energy confinement times, with comparatively little change

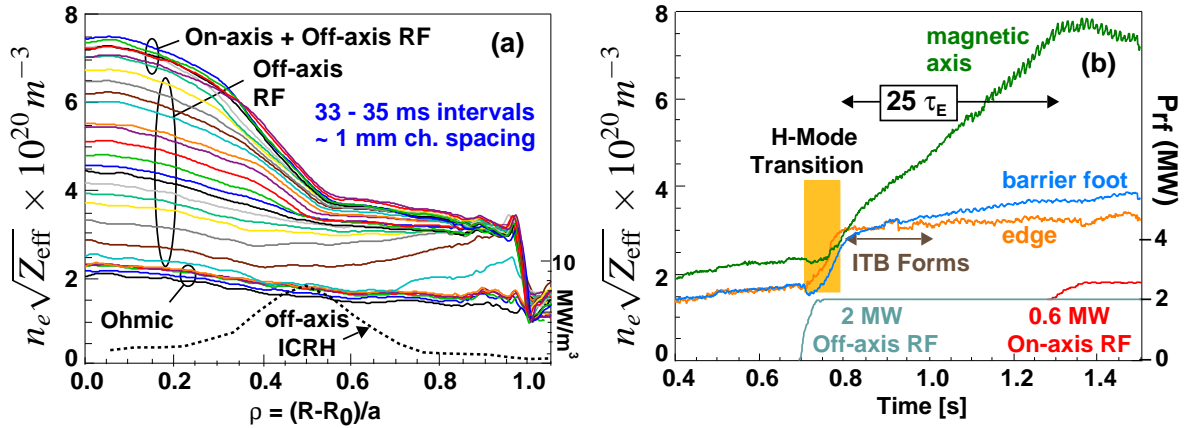


FIG. 1. (a) Visible brehmstraahlung emission profiles and off-axis ICRF heating profile from TORIC (TRANSP). (b) Density evolution and applied ICRF heating power.

the temperature profile. C-Mod densities have exceeded  $10^{21} \text{ m}^{-3}$  in ITB cases. The ITB forms with nearly equal ion and electron temperatures, and without core fueling, reversed magnetic shear, large Shafranov shift, significant impurity content ( $1 < Z_{\text{eff}} < 2$  most of the time), hot ions (the RF tail density is of order 5% or less of the electron density), or external torques. The rate of rise of the density, and the strength of density peaking and impurity accumulation inside the ITB foot can be controlled by applying on-axis ICRF heating power [5, 9]. Recent results [9] include observation of a sharp threshold for ITB formation as a function of the ICRF resonance position, on both low and high field sides. No hysteresis is observed in the threshold magnetic field. The ITB foot position is almost linearly increasing with  $I_p B_r$  or  $q_{95}$ . Although C-Mod H-Mode plasmas display significant intrinsic toroidal rotation up to 80 km/s, the velocity profile [10] is relatively flat inside the ITB after several energy confinement times. Preliminary calculations suggest that  $E \times B$  shear may play a role near the ITB foot, in the early stages of formation [1].

The evolution of the density profiles [5], together with the applied heating power, are shown in FIG. 1 (here  $B_0 = 4.5 \text{ T}$ ,  $I_p = 0.8 \text{ MA}$ ). Immediately following the injection of 2 MW off-axis hydrogen minority ICRH at 80 MHz on the high field side, the transition to EDA H-Mode occurs (0.7-0.8 s). The electron density profiles are well resolved, up to a factor  $\sqrt{Z_{\text{eff}}}$ , by a 218 channel CCD based visible bremsstrahlung emission spectroscopy array, yielding  $\sim 1$  mm channel spacing and sub-millisecond sampling [11]. Following the H-Mode transition, the core density rises steadily inside the half-radius, for tens of energy confinement times, until it is arrested by the application of 0.6 MW of on-axis ICRH. The temperature profile remains relatively fixed while the density peaks. Transport analysis shows the ion thermal diffusivity approaches neoclassical values inside the ITB foot [8]. In early cases, on-axis heating in excess of 1 MW resulted in a collapse of the ITB. Recently, however, the full available source power (2.3 MW off-axis, 1.7 MW on-axis) has been applied to maintain the ITB in steady state.

The  $Z_{\text{eff}}$  profile can be obtained in conjunction with Thomson scattering measurements of the electron density. The core Thomson scattering system was recently upgraded from 8 to 12 channels. Fits to this data show  $Z_{\text{eff}}$  is close to unity outside the ITB and that  $Z_{\text{eff}}$  increases with time inside the ITB foot. This impurity accumulation, which may result from the neoclassical impurity pinch driven by the density gradient [12], is arrested with small amounts of on-axis ICRH heating [5]. It is worth pointing out that our simulations show the electron thermal, impurity particle, electron particle, and ion thermal diffusivities are ordered  $\chi_e > D_I > D_e > \chi_i$ . This suggests that TEM turbulence is an effective means of removing impurities without

degrading ion thermal energy content, other than through the electron channel.

## 2. Gyrokinetic Stability Analysis

The temporal evolution of the maximum linear growth rate in the ITB, calculated using the GS2 flux-tube gyrokinetic code [4, 13], aided by automated data preparation and plotting tools [14, 1] is shown FIG. 2. Following the transition to H-Mode, the ITB formation phase is characterized by a slow and steady shortening of the density gradient scale length at  $\rho = 0.4$ , where  $\rho = \sqrt{\text{norm. tor. flux}} \sim r/a$ . The temperature profile inside the half-radius is near marginal stability with respect to toroidal ITG modes during this early phase, which are either weakly growing or stable within experimental errors. Recent discharges have excellent ECE and Thomson scattering profile data, which should clarify the early phase microstability analysis of this older data, carried out in some detail in Ref. [15]. The temperature profiles for this discharge were obtained from a few off-axis X-ray emission data points, together with an on-axis ion temperature adjusted to match the measured neutron rate. The results described here, for the late phase of the discharge, are relatively insensitive to the temperature profile shape. Radial electric field shear may play a role near the ITB foot in this early phase, but insufficient profile data exists for quantitative analysis. Late in time, the toroidal velocity has slowed, and the profile is relatively flat. The  $E \times B$  shearing rate, using a numerical neoclassical calculation of the poloidal velocity [16], is negligible late in time. As the density gradient steepens, it eventually crosses the stability threshold for trapped electron modes. This occurs near 1.0 seconds, signified by the sudden increase in linear growth rate, and the change in sign of the phase velocity from ion to electron direction.

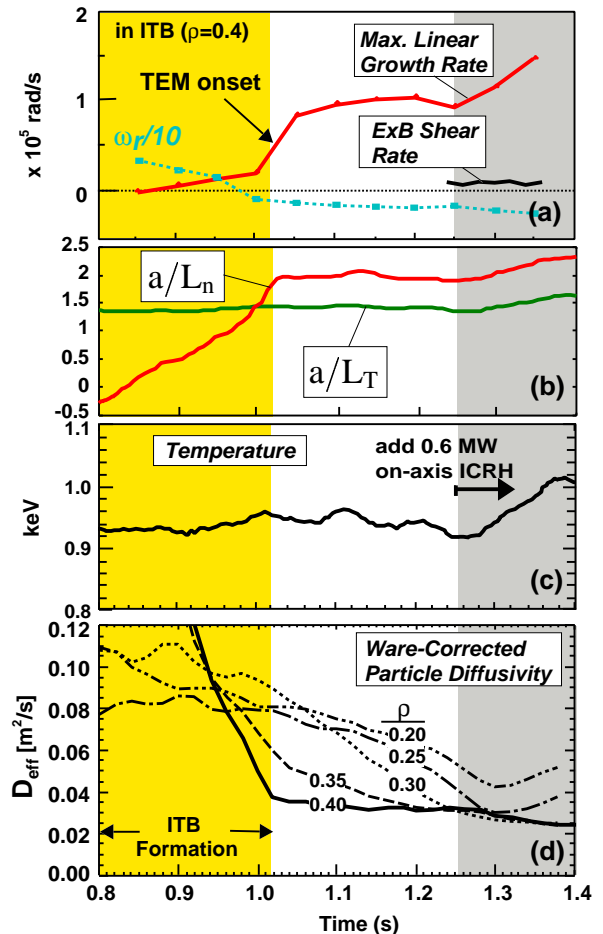


FIG. 2. (a) Growth rate and frequency from GS2 shows TEM onset at 1.0 s, (b) Inverse density and temperature gradient scale lengths, (c) Temperature increases during on-axis ICRH, (d) Effective particle diffusivity from transport analysis.

Trapped electron modes drive significant particle transport relative to toroidal ITG modes, whose density response remains close to adiabatic. The ITB formation phase ends at each radius at the same time that the TEM become locally unstable. Simultaneously, the Ware-corrected particle diffusivity from transport analysis stops decreasing. Similar behavior is seen at later times, closer to the magnetic axis. There, the TEM do not get excited until on-axis heating is applied at 1.25 seconds. When the on-axis heating is applied, a corresponding increase in temperature, TEM growth rate, and inferred particle diffusivity are apparent.

In the absence of core particle sources, the continuity equation is simply  $\partial n_e / \partial t + \nabla \cdot (\Gamma_{\text{Ware}} - D_{\text{eff}} \nabla n_e) = 0$ . Utilizing the calculated neoclassical flux  $\Gamma_{\text{Ware}}$  [17, 18], together with the 218 channel visible bremsstrahlung measurements of  $n_e \sqrt{Z_{\text{eff}}}$ , we invert this equation, in general magnetic geometry, to obtain the the Ware-corrected effective particle diffusivity,  $D_{\text{eff}}$ . The toroidal electric field was obtained from the TRANSP solution to the poloidal magnetic field diffusion equation, using neoclassical resistivity, constrained to match the EFIT reconstructed separatrix and total plasma current, with a flat  $Z_{\text{eff}}$  profile. The neoclassical pinch is sufficient to yield  $D_{\text{eff}} > 0$  over the plasma cross-section, for all times. This confirms that the neoclassical pinch is sufficient to account for the density rise [19]. Sawtooth heat pulse analysis suggests the ITB consists of a narrow region of reduced transport [5], while profiles of  $D_{\text{eff}}$  show a broader depression centered at  $\rho = 0.4$  [1].

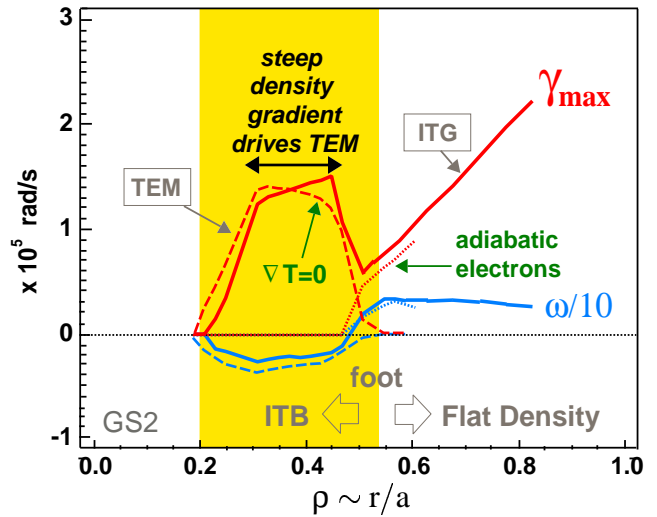


FIG. 3. Linear stability analysis from GS2, showing a purely density gradient driven TEM inside the ITB, with off-axis and on-axis ICRH, at 1.34 s.

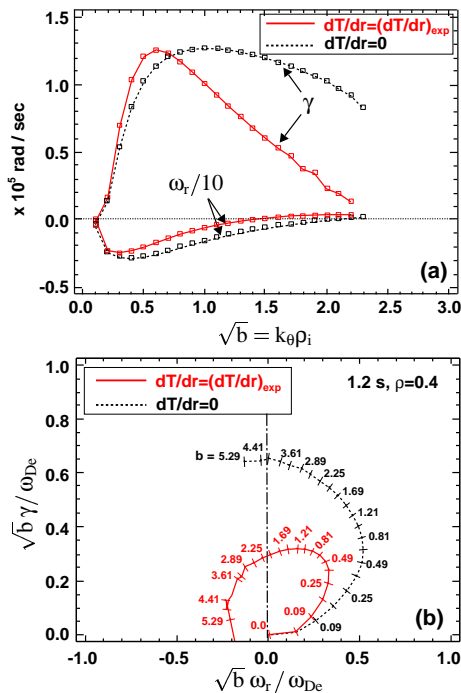


FIG. 4. (a) Linear growth rate spectrum in the ITB, (b) Root locus with parameter  $\sqrt{b} = k_{\theta} \rho_i$ , with  $\omega_{De} = \omega_{*e} L_n / R$ .

FIG. 3 shows the radial profile of the maximum linear growth rate calculated in 50 GS2 runs, at 1.34 seconds, during on-axis ICRH. A strongly growing mode appears inside the ITB foot, with a phase velocity in the electron direction ( $\omega_r < 0$ ). Artificially turning off the temperature gradient has little effect inside the ITB foot, showing the mode is driven solely by the density gradient. The mode disappears when only adiabatic electrons are included, and is therefore associated with trapped electrons. Outside the ITB foot, the phase velocity is in the ion diamagnetic direction, and the growth rate is not significantly reduced with adiabatic electrons. This toroidal ITG mode has a growth rate increasing with minor radius as is typical of H-Mode plasmas.

The linear growth rate spectrum for the TEM peaks at  $k_{\theta} \rho_i = 0.6$ , similar to toroidal ITG modes, as shown in FIG. 4. Turning off the temperature gradient extends the spectrum to shorter wavelengths. The root-locus diagram in FIG. 4 shows that a class of purely growing modes exist, which cannot be resonant. The spectrum appears to contain both resonant [20, 21] and non-resonant [22] TEM. The following approximate expression for the growth rate in the fluid limit can be readily derived, starting from the kinetic ion response given in Eq. (2) of Ref. [23], and expanding the trapped electron response of Ref. [21] for  $\omega_{De} / \omega \ll 1$ , in the local approximation, for

$\eta_i \gg 1$  and  $\eta_i \ll 1$ , where  $\eta_i = d \ln T_i / d \ln n$ ,  $b_i = k_\theta^2 \rho_i^2 / 2$ ,  $n_{eT}$  is the trapped electron density,  $n_i = n_e = n$ , and  $T_i = T_e$  have been assumed for simplicity, and  $g_{\text{eff}} = v_{\text{thi}}^2 / R$ , yielding  $\gamma \simeq k_\theta \rho_i (g_{\text{eff}} / L_n)^{1/2} \{ ([1 + \eta_e] n_{eT} / n + \eta_i) / (1 - n_{eT} / n + b_i) \}^{1/2}$ . This simplified growth rate [1] somewhat describes relative importance of the ITG and TEM growth rates well above threshold.

We have used several hundred linear GS2 simulations to map out the stability diagram in  $a/L_n$  vs  $a/L_T$  space, fixing other parameters at their  $\rho = 0.4$ ,  $t = 1.20$  s values. The stable and unstable regions for toroidal ITG modes, toroidal ITG modes with additional trapped electron drive, and trapped electron modes are shown in FIG. 5. For parameters characterizing  $\rho = 0.4$  at 1.20 seconds, the TEM threshold was fit by a line,  $(a/L_n)_{\text{crit}} = 0.4 + 0.83(a/L_T)$  for  $0 \leq a/L_T \leq 1.45$ , and a constant  $(a/L_n)_{\text{crit}} = 1.6$  for  $a/L_T \geq 1.45$ . Because  $a/L_T \geq 1.5$  for  $t \geq 0.80$  seconds, on-axis heating does not affect the TEM linear critical density gradient.

As shown in FIG. 5, the ITB trajectory follows the stability boundary for toroidal ITG modes until the density profile begins to peak. Just after the H-Mode transition, the density gradient is briefly inverted, placing the trapped electrons in ‘‘good curvature.’’ The destabilizing influence of trapped electrons on the toroidal ITG mode is removed, coincident with the onset of density peaking. The ITB then follows a trajectory of constant  $a/L_T$ . Shortly after crossing the TEM stability boundary, the trajectory stagnates with  $a/L_n \sim 2$ .

### 3. Nonlinear Gyrokinetic Turbulence Simulations

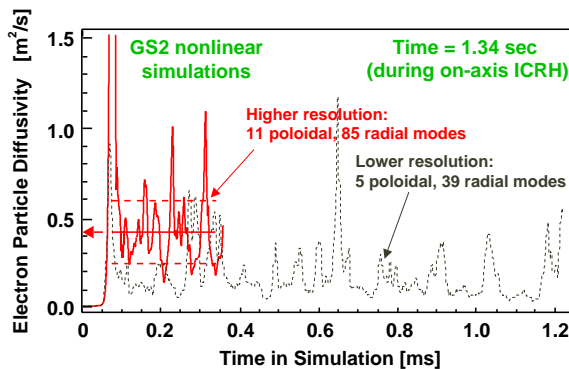


FIG. 6. High and low resolution simulations: 11 vs. 5 poloidal modes.

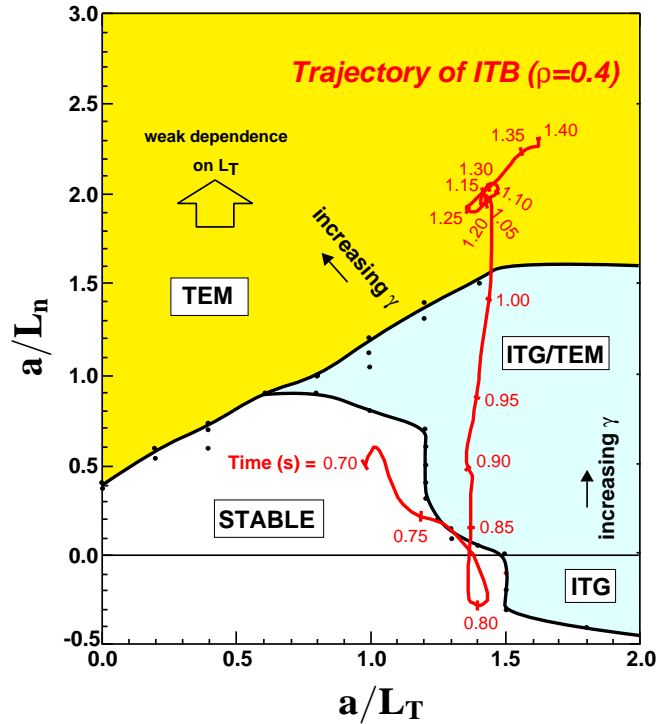


FIG. 5. Trajectory of ITB radius through stability diagram shows that profiles initially follow ITB marginal stability boundary. Density peaks with constant temperature gradient until trajectory stagnates shortly after crossing TEM threshold.

The extended poloidal wavenumber spectrum characteristic of TEM turbulence requires more poloidal modes than the usual spectral simulations of toroidal ITG modes. Together with eigenfunctions that extend considerable distances along magnetic field lines, this requires an extended radial modenummer spectrum. Our convergence studies indicate that roughly eight times as many radial modes are required as poloidal modes for this case. Further, at least 11 poloidal modes ( $k_\theta \rho_i$  values) are required. Simulations running roughly 300  $\mu\text{sec}$ , with 11 poloidal and 85 radial modes, require 24 hours

on 2640 processors on an IBM SP computer system. Using significantly less radial modes resulted in lower transport and an erroneously large pinch in the early ITG/TEM phase. FIG. 6 compares high and low resolution simulations at 1.34 seconds (during on-axis ICRH), at the ITB radius  $\rho = 0.4$ . A flat  $Z_{\text{eff}}$  profile was assumed, taking the density gradient scale length directly from the visible Bremsstrahlung emission profile. Even the longer duration simulation shows large, infrequent bursts of particle flux occur throughout the simulation. The lower resolution case shows there is no long-term drift in the turbulent particle flux, so that extremely long run times are unnecessary for the expensive high resolution case.

We have found a new nonlinear upshift of the critical density gradient for onset of TEM turbulence [1], shown in FIG. 7 LEFT. In this scan of  $a/L_n$ , holding all other parameters fixed, significant transport does not appear until  $a/L_n$  exceeds 1.35, while the threshold for linear growth is 1.2. We have carried out more detailed and efficient studies by modifying the DIII-D L-Mode based ‘‘Cyclone base case’’ [3]. We include trapped electrons and just enough electron-ion collisions  $v_{ei}a/v_{thi} = 0.01$ , with corresponding ion-ion collisions, to avoid spurious results from collisionless simulations. The temperature gradient is set to zero, and only  $a/L_n$  is varied.

FIG. 7 RIGHT shows that a zonal-flow dominated, nonlinearly quasi-stable state exists above the linear threshold,  $R/L_n = 1.44$ . The zonal flow potential for  $R/L_n = 1.8$  remains above that of the primary modes following the initial explosive burst. As the density gradient increases, quasiperiodic, then turbulent behavior appears. All three cases fall within the nonlinearly quasi-stable regime. This nonlinear upshift is analogous to the Dimits shift in the critical ion temperature gradient for toroidal ITG modes [3], reconfirmed in the ITG case with non-adiabatic electrons [24].

FIG. 7 RIGHT shows that a zonal-flow dominated, nonlinearly quasi-stable state exists above the linear threshold,  $R/L_n = 1.44$ . The zonal flow potential for  $R/L_n = 1.8$  remains above that of the primary modes following the initial explosive burst. As the density gradient increases, quasiperiodic, then turbulent behavior appears. All three cases fall within the nonlinearly quasi-stable regime. This nonlinear upshift is analogous to the Dimits shift in the critical ion temperature gradient for toroidal ITG modes [3], reconfirmed in the ITG case with non-adiabatic electrons [24].

#### 4. Comparison of Nonlinear Simulations with Experiment

The high resolution simulations reproduce the particle and thermal transport inferred from transport analysis in the ITB, at  $\rho = 0.4$  and  $t=1.2$  s, as shown in FIG. 8. At the same time, the particle flux balances the neoclassical Ware pinch in the ITB, resulting in a stable equilibrium. The density gradients and  $Z_{\text{eff}}$  gradient artificially and self-consistently scanned within range of experimental errors;  $a/L_{ne} = 1.95$  corresponds to a flat  $Z_{\text{eff}}$  profile, while  $a/L_{ne} = 1.3$  corresponds to  $L_{Z_{\text{eff}}} = L_{ne}$ . This range is based on more recent Thomson scattering data. The abscissa on this plot is analogous to time. At early times, when  $\eta_e > 2$ , circulating particles are observed to flow inward as a result of a resonant effect [25]. This inflow is present in our simulations, 80%

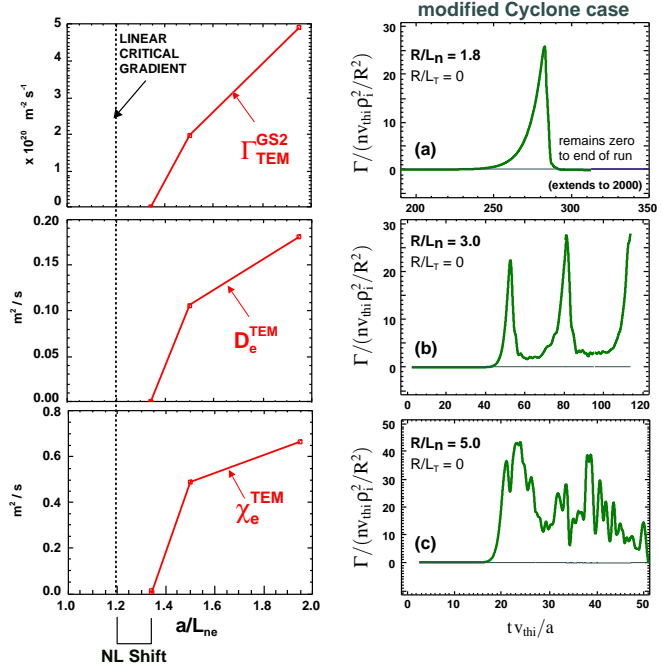


FIG. 7. LEFT: Nonlinear upshift of TEM critical density gradient using ITB parameters ( $\rho = 0.4$ , 1.20 s). (a) Electron particle flux, (b) particle diffusivity, (c) electron thermal diffusivity. RIGHT: Nonlinear simulations for modified Cyclone base case, above linear critical gradient ( $R/L_n = 1.44$ ). (a)  $R/L_n = 1.8$ , (b)  $R/L_n = 3.0$ , (c)  $R/L_n = 5.0$

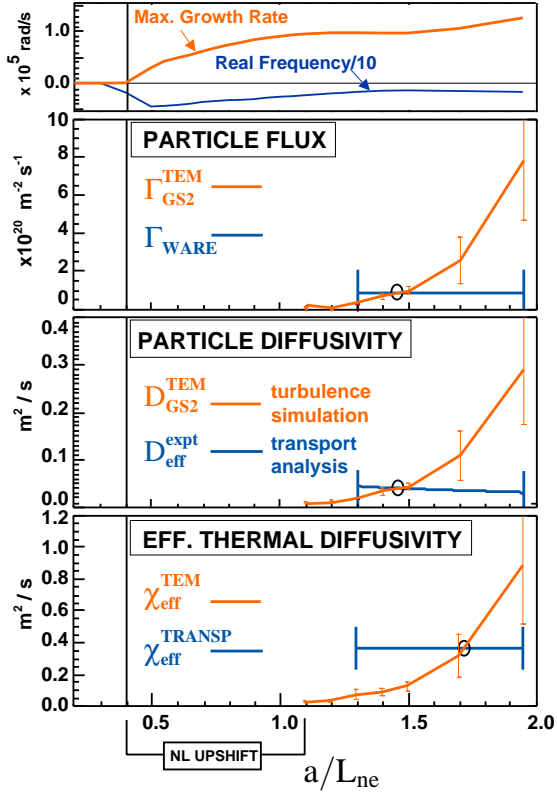


FIG. 8. Comparison of simulations (orange) with transport analysis (blue) in the ITB, at  $\rho = 0.4$ ,  $t=1.2$  s. Vertical rms standard error bars roughly show intermittency (non-Gaussian PDF).

due to circulating particles, but has negligible magnitude. Recent European work has emphasized a different thermodiffusive pinch, obtainable from fluid equations [26]. However, this type of pinch is not seen in our simulations of these relatively collisional cases.

## 5. Mechanism for ITB Control with On-axis ICRF Heating

We have established that the TEM turbulent outflow and collisional inflow are in balance in the ITB. We have carried out temperature scans in the simulations to establish whether the temperature scaling of this equilibrium could account for the density gradient control with on-axis ICRH. FIG. 9(a) shows that the collisionality dependence of the linear growth rate is saturated, resulting in little temperature scaling from collisionality. Consistently, FIG. 9(b) shows the electron particle diffusivity displays essentially gyroBohm temperature scaling (here  $\rho_* \simeq 1/200$  suggests the local limit, gyroBohm scaling[27]). Combining this with the temperature dependence of the plasma resistivity and Ware pinch leads to

$$\frac{\partial n_e}{\partial t} + \nabla \cdot \left\{ \Gamma_0^{\text{TEM}} \left( \frac{T}{T_0} \right)^{3/2} + \Gamma_0^{\text{Ware}} \left( \frac{T}{T_0} \right)^{-1/2} \right\} = 0,$$

illustrating a sensitive mechanism for control of the density rate of rise, by on-axis ICRH, via the temperature dependence.

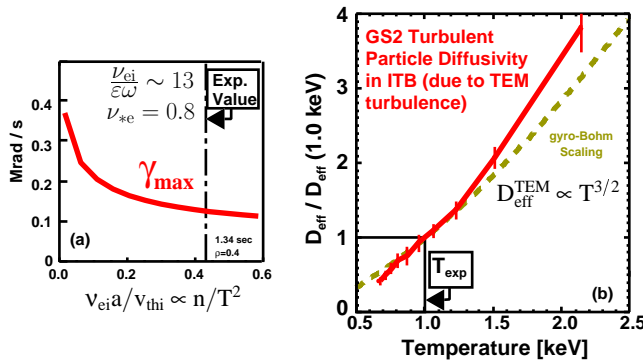


FIG. 9. (a) Collisionality dependence of linear growth rate is saturated in ITB, (b) Temperature scaling of simulated transport in ITB is gyro-Bohm, with collisionality subdominant.

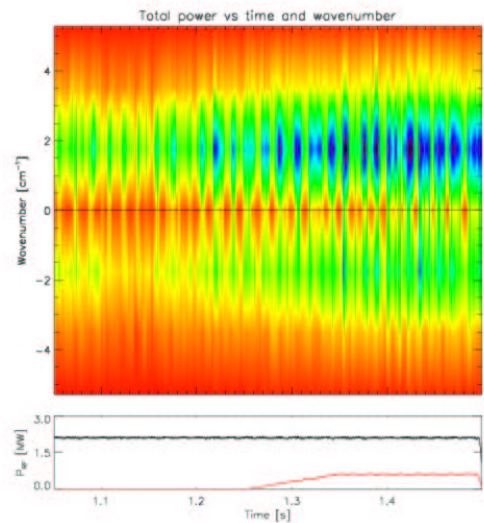


FIG. 10. Wavenumber spectrum vs. time from PCI for the same range of wavelengths and frequencies found in the nonlinear GS2 TEM simulations.

## 6. Phase Contrast Imaging Fluctuation Data

Preliminary comparisons of our nonlinear simulations with line-integrated data from Phase Contrast Imaging (PCI) [28] are shown in FIG. 10 for the discharge analyzed in this paper. The data clearly shows a marked increase of fluctuation amplitude during on-axis ICRH, for modes already present, as the simulations predict. The simulated frequency spectrum falls between 0 and  $\sim 60$  kHz, while the PCI data is shown from 10-60 kHz, avoiding the quasi-coherent mode near 110 KHz. The simulated poloidal wavenumber spectrum is downshifted from the linear spectral peak, in rough agreement with PCI (for  $\rho = 0.4$ , PCI sees primarily poloidal wavenumbers), which sees a peak at  $k_\theta \simeq 2 \text{ cm}^{-1}$ . The interval of the large scale bursts is comparable to the sawtooth period. Recently, PCI has increased the number of channels from 12 to 32, its sample rate from 1 MHz to 10 MHz, and its time window by a factor of six.

## References

- [1] ERNST, D. R. et al., Phys. Plasmas **11** (2004) 2637.
- [2] ERNST, D. R. et al., Bulletin of the American Physical Society **47** (2002) 139.
- [3] DIMITS, A. M. et al., Phys. Plasmas **7** (2000) 969.
- [4] DORLAND, W. D. et al., Phys. Rev. Lett. **85** (2000) 5579.
- [5] WUKITCH, S. J. et al., Phys. Plasmas **9** (2002).
- [6] RICE, J. E. et al., Nucl. Fusion **41** (2001) 277.
- [7] FIORE, C. L. et al., Phys. Plasmas **8** (2001) 2023.
- [8] FIORE, C. L. et al., Phys. Plasmas **11** (2004) 2480.
- [9] FIORE, C. L. et al., To appear in Plasma Phys. Contr. Fusion SPECIAL ISSUE: Invited papers from the 31st EPS Conference on Plasma Physics (London, UK, 28 June-2 July, 2004).
- [10] RICE, J. et al., Nucl. Fusion **44** (2004) 379.
- [11] MARMAR, E. et al., Rev. Sci. Instrum. **72** (2001) 940.
- [12] HIRSHMAN, S. P. et al., Nucl. Fusion **21** (1981) 1079.
- [13] KOTSCHENREUTHER, M. et al., Comp. Phys. Comm. **88** (1995) 128.
- [14] ERNST, D. R. et al., Phys. Plasmas **7** (2000) 615.
- [15] REDDI, M. H. et al., 30th EPS Conf. on Contr. Fusion and Plasma Phys., St. Petersburg, 7-11 July 2003 ECA Vol. 27, P-3.98.
- [16] ERNST, D. R. et al., Phys. Plasmas **5** (1998) 665.
- [17] HINTON, F. L. et al., Rev. Mod. Phys. **48** (1976) 239.
- [18] HIRSHMAN, S., Physics of Fluids **21** (1978) 1295.
- [19] BONOLI, P. T. et al., Bull. Am. Phys. Soc. **46** (2001) 54.
- [20] KADOMTSEV, B. B. et al., Sov. Phys.-JETP **24** (1967) 1172, Sov. Phys.-Dokl. **14** (1969) 470, and in *Reviews of Plasma Physics*, edited by LEONTOVICH, M., volume 5, page 249, Consultants Bureau, New York, 1970.
- [21] ADAM, J. C. et al., Phys. Fluids **19** (1976) 561.
- [22] COPPI, B. et al., Phys. Lett. A **49A** (1974) 36, Phys. Rev. Lett. **33** (1974) 1329, Nucl. Fusion **17** (1977) 969, and Phys. Fluids B **2** (1990) 2322.
- [23] TANG, W. M. et al., Phys. Fluids **29** (1986) 3715.
- [24] PARKER, S. E. et al., Phys. Plasmas **11** (2004) 2594.
- [25] HALLATSCHKE, K. et al., Bull. Am. Phys. Soc. **47** (2002) 135, Paper GI1.005.
- [26] GARBET, X. et al., To appear in Plasma Phys. Contr. Fusion SPECIAL ISSUE: Invited papers from the 31st EPS Conference on Plasma Physics (London, UK, 28 June-2 July, 2004).
- [27] CANDY, J. et al., Phys. Plasmas **11** (2004) L25.
- [28] MAZURENKO, A. et al., Phys. Rev. Lett. **89** (2002) 225004.